Biosensors and Bioelectronics 126 (2019) 743–750

Contents lists available at ScienceDirect

Biosensors and Bioelectronics

journal homepage: www.elsevier.com/locate/bios

Color-sensitive and spectrometer-free plasmonic sensor for biosensing applications

Seunguk Kim[a], Youngjin Lee[b], Jae Yeon Kim[c], Jae Hoon Yang[a], Hyuk-Jun Kwon[a], Jae Youn Hwang[a], Cheil Moon[c], Jae Eun Jang[a,*]

[a] Department of Information and Communication Engineering, Daegu Gyeongbuk Institute of Science & Technology (DGIST), Daegu 42988, Republic of Korea
[b] Samsung Display, Asan 31454, Republic of Korea
[c] Department of Brain and Cognitive Sciences, Daegu Gyeongbuk Institute of Science & Technology (DGIST), Daegu 42988, Republic of Korea

ARTICLE INFO

Keywords:
Plasmonic sensor
Nanohole arrays
Spectrometer-free
Color-sensitive analysis
Image processing
Biosensing

ABSTRACT

A color-sensitive and spectrometer-free sensing method using plasmonic nanohole arrays and the color components, L*, a*, and b*, of the CIELAB defined by the international commission on illumination (CIE) is introduced for the analysis of optically transparent materials in the visible range. Spectral analysis based on plasmonic nanoparticles or nanostructures can be applied to real-time bio-detection, but complex optical instrumentations and low spatial resolution have limited the sensing ability. Therefore, we take an advantage of color image processing instead of spectral analysis which induces the distinctive color information of plasmonic nanohole arrays with different transparent materials. It guarantees high spatial resolution which is essential to bio-detection such as living cells. To establish our sensing platform, the color components, L*, a*, and b*, were extracted from photo images by an image sensor, statistically processed using a JAVA program, and finally utilized as three individual sensing factors. Additionally, our study on a correlation between the spacing of plasmonic sensors and the color sensitivity to the refractive index reveals geometrically optimal conditions of nanohole arrays. The weighted mean calculation with the three individual sensing factors offers an enhanced distinction of the optical difference for transparent materials. In this work, a color sensitivity of 156.94 RIU^{-1} and a minimum mean absolute error of 1.298×10^{-4} RIU were achieved. The difference in the refractive index can be recognized up to 10^{-4} level with the suggested sensing platform and the signal process. This unique color-sensitive sensing method enables a simple, easy-to-control, and highly accurate analysis without complicated measurement systems including a spectrometer. Therefore, our sensing platform can be applied as a very powerful tool to in-situ label-free bio-detection fields.

1. Introduction

The surface plasmonic effect, which is the resonant oscillation of light and free electrons on the surface of metal, has been studied and used in various applications due to its very distinctive and interesting phenomenon (Beck et al., 2009; Burgos et al., 2013; Lee et al., 2017; Park et al., 2014; Tseng et al., 2017). In particular, this unique optical property has given great inspiration to emerging surface plasmon resonance (SPR) sensing techniques because the resonance and its spectral characteristics are highly sensitive to the change in the surrounding environment such as dielectric and metal interfaces (Chen et al., 2015; Homola et al., 2002; Kabashin et al., 2009; Lin et al., 2017; Na et al., 2018; Yanik et al., 2010; Zhang et al., 2015; Zhou et al., 2016). Most of all, real-time and label-free measurement based on SPR can make a bioanalysis more time-effective and less invasive. However, despite the achievement in high sensitivity (Liu et al., 2018), relatively simple fabrication process (Jackman et al., 2016), and large sensing area (Baquedano et al., 2017), such analysis, based on spectral shift still needs expensive, complex, and immovable optical instrumentations which limit the practical utilization in point-of-care diagnostics.

In recent, the use of a charge coupled device (CCD) camera or a complementary metal-oxide-semiconductor (CMOS) imager as a sensor in measurement system has been considered that it is a promising alternative to solve the problems of spectrometer-based analysis. The detection of the light intensity change is one of representative imager-based analysis methods. Screening of biomaterials by dual color filters

* Corresponding author.
E-mail addresses: kissuluv@dgist.ac.kr (S. Kim), youngjin.lee@samsung.com (Y. Lee), awisekim@dgist.ac.kr (J.Y. Kim), didwo0830@dgist.ac.kr (J.H. Yang), hj.kwon@dgist.ac.kr (H.-J. Kwon), jyhwang@dgist.ac.kr (J.Y. Hwang), cmoon@dgist.ac.kr (C. Moon), jang1@dgist.ac.kr (J.E. Jang).

https://doi.org/10.1016/j.bios.2018.11.048
Received 11 September 2018; Received in revised form 14 November 2018; Accepted 27 November 2018
Available online 07 December 2018
0956-5663/

is designed to enhance the signal-to-noise ratio and induce a large resonance spectral intensity difference (Chang et al., 2011; Coskun et al., 2014). Adding a computing process enables higher throughput and multiplexed detection. The concentration and binding events of biomaterials are obtained by over 150,000 plasmonic sensors and computational on-chip imaging (Cetin et al., 2014). The machine learning framework reduces the refractive index prediction errors and shows statistically stable read-out results (Ballard et al., 2017). To obtain high intensity sensitivity from a plasmonic sensor, the line width of the characteristic spectrum should be reduced. Due to the reason, some studies have endeavored to develop narrow and sharp resonance peaks (Li et al., 2015; Zafar and Salim, 2015). However, for spectrometer-free sensing platforms based on a change in the spectral intensity, there is a trade-off between the intensity sensitivity and the sensing range. The intensity sensitivity improves by decreasing the line width; however, the measurable refractive index value becomes more limited. To enhance the intensity sensitivity, complicated strategy in material, structure, fabrication, and measurement are required. Meanwhile, in recent, color-sensitive imaging process has been suggested as an alternative sensing method. Metallic nanoparticles (NPs) show potential to be utilized for bio-detection. In dark-field mode of an optical microscope, color difference occurs when the biomaterials are attached to the NPs because the resonance color differs according to the size of the NPs (Im et al., 2014). Plotting the spectrum and identifying the resonance shift using the NPs and the HSV (hue, saturation, and value) which is one of the color coordinate systems enables detecting antigen-antibody immune process without a spectrometer (Sriram et al., 2018). Color-coded detection by constructing the relationship between the HSI (hue, saturation, and intensity) color components and the refractive index represents that the color of NPs could act as a sensing factor (LingáZheng et al., 2016). However, the NPs based colorimetric analysis has suffered from prediction with a large error and a low accuracy due to significantly small sensing area. In this sense, plasmonic nanostructures with relatively large sensing area (~over several ten or hundred micrometers) have been expected to solve the problem. The refractive index sensing based on CIELAB with the anodic aluminum oxide template consisted of periodically arrayed gold nanoholes showed higher sensitivity and more reliable prediction (Bae et al., 2015). Despite efforts to develop color-sensitive analysis methods, the detecting ability has been still poorer compared to other platforms because most studies considered only one component of the color space (hue value of HSV/HSI or Euclidean distance of CIELAB) as a sensing factor and used simple calculation, such as the arithmetic mean, to obtain sensing results. Therefore, by utilizing all color components as sensing factors and applying more effective mathematical process for accurate prediction, we could obtain significantly enhanced sensitivity and reduced sensing error in color-sensitive analysis.

In this paper, we demonstrate a sensitive but simpler sensing for the optical characteristics of transparent materials using plasmonic sensors and color signal processing based on the color components, L*, a*, and b*, of CIELAB. Because our color-sensitive platform enables spectrometer-free sensing with only a CCD camera and collects the color information of each pixel, it guarantees quite a high-throughput, real-time analysis, and label-free bio-detection. The prediction using linear correlation models of the color components and the refractive index shows good agreement with a real value. In addition, the weighted mean calculation drastically improves the sensing ability of our platform. A large population of sensing pixels and a linear sensitivity offer a statistically stable and reliable prediction with very little errors.

2. Materials and methods

2.1. Fabrication and design of the plasmonic sensors

As the first step of the fabrication of the plasmonic sensors, 70-nm-thick aluminum was thermally evaporated and deposited onto a glass substrate at a rate of 1 Å/s. Then, PMMA (950 kDa, 4% in Anisole) was spin-coated at a rate of 4000 rpm. After the electron beam lithography process (RAITH-150TWO) with an accelerating voltage of 20 kV, nanohole patterns were formed on the aluminum layer by inductively coupled plasma and reactive ion etching after the development process. An ashing system was used to remove the residual polymers on the aluminum surface. As a result, a total of nine plasmonic sensors was obtained which consisted of hexagonal nanohole arrays with various spacing and diameter conditions. The spacing between the nearest holes that make up the nanohole array in each sensor was designed to be from 275 to 475 nm in 25 nm increments. The diameter of the holes was 0.4 times the spacing (110–190 nm in 10 nm increments). The nine plasmonic sensors with a square area of 50 μm × 50 μm were each 150 μm apart. Optical transmission images, scanning electron microscope images, and transmission spectra of the fabricated plasmonic sensors with the hexagonal nanohole arrays are shown in Fig. 2.

2.2. Mathematical models of CIELAB

CIELAB is widely used as a representative color space together with RGB (red, green, and blue), CMYK (cyan, magenta, yellow, and black), HSB (hue, saturation, and brightness), and the like. In particular, it expresses colors in one lightness (L*) and two color terms (a* for green-to-red and b* for blue-to-yellow) which work independently of each other. The orthogonality of L*, a*, and b* enables the three-dimensional representation of the colors and eventually provides the three sensing factors in our sensing platform. In fact, CIELAB originated from the CIEXYZ color space first devised to convert the distributions of the electromagnetic spectrum in the visible light region into a numerical expression and to standardize them quantitatively. The component X, Y, and Z of CIEXYZ can be described as follow:

$$X = \sum_{\lambda} X_{\lambda} = \sum_{\lambda} K \int_{\lambda}^{\lambda+1} I(\tau)T(\tau)\bar{x}(\tau)d\tau \tag{1}$$

$$Y = \sum_{\lambda} Y_{\lambda} = \sum_{\lambda} K \int_{\lambda}^{\lambda+1} I(\tau)T(\tau)\bar{y}(\tau)d\tau \tag{2}$$

$$Z = \sum_{\lambda} Z_{\lambda} = \sum_{\lambda} K \int_{\lambda}^{\lambda+1} I(\tau)T(\tau)\bar{z}(\tau)d\tau, \tag{3}$$

where K is a scaling constant; I(λ) is an illumination spectral power distribution, and T(λ) is a spectral transmittance measured from the targeted sample. $\bar{x}(\lambda)$, $\bar{y}(\lambda)$, and $\bar{z}(\lambda)$ are color matching functions. The interval of integration of each color component is limited to the visible wavelength range from 400 to 780 nm. The color components, L*, a*, and b*, of CIELAB are derived from a combination of X, Y, and Z as below:

$$L^* = 116f\left(\frac{\sum_{\lambda} Y_{\lambda}}{Y_n}\right) - 16 \tag{4}$$

$$a^* = 500\left[f\left(\frac{\sum_{\lambda} X_{\lambda}}{X_n}\right) - f\left(\frac{\sum_{\lambda} Y_{\lambda}}{Y_n}\right)\right] \tag{5}$$

$$b^* = 200\left[f\left(\frac{\sum_{\lambda} Y_{\lambda}}{Y_n}\right) - f\left(\frac{\sum_{\lambda} Z_{\lambda}}{Z_n}\right)\right], \tag{6}$$

where X_n, Y_n, and Z_n are the CIEXYZ tristimulus constant values. $f(t)$ is given as $\sqrt{t}$ ($t > 0.0089$) and $7.7870t + 0.1379$ ($t \leq 0.0089$).

2.3. Sensing platform set-up

To detect the different refractive indices of transparent materials using our color-sensitive and spectrometer-free sensing platform, NaCl solutions with various concentrations were prepared. Non-polarized white light normally incident onto the plasmonic sensors totally immersed in the solutions was coupled with localized surface plasmons at

the interface between the nanohole arrays and dielectric (NaCl solution) media. A CCD camera (ProgRes Gryphax Naos, Jenoptik) took images of the plasmonic sensors (Fig. S1). Then, the color components from 200 × 200 pixels per sensor were extracted by a JAVA program. Based on the experimentally observed variations of L*, a*, and b*, the color sensitivity to the refractive index and the prediction error expressed as the mean absolute error (MAE) were calculated. In addition, linear correlations between the concentration of the NaCl solutions and the color components at each plasmonic sensor were obtained. Finally, the weighted mean calculation with the predicted refractive indices and MAE values of individual sensing factors, L*, a*, and b*, was used to improve the sensing ability. To evaluate and validate our new sensing method theoretically, the spectral property of the sensors was measured by an optical spectrometer (DALSA PRO-5200) with a 1 nm resolution and used as the transmission spectral factor in Eqs. (1)–(3).

3. Results and discussion

3.1. Working principle of the analysis system based on plasmonic sensors

A schematic diagram for the analysis system and the concept of color image processing are presented in Fig. 1. In general, transparent materials are hard to be recognized each other through an optical microscope due to their colorless for visible light. However, their own characteristic colors are detectable when they are observed with plasmonic sensors (Fig. 1a). This is due to the change of plasmonic mode on the plasmonic sensor by the materials, even though the materials are transparent in visible range. If each pixel color information obtained from an optical image by an imager, a CCD camera, is analyzed, the color analysis results enable for the detection of transparent materials with high spatial resolution. In here, the real size of image is around 60 μm × 60 μm and the image pixels are 5000 × 5000, so that the ideal minimum resolution is 0.012 μm × 0.012 μm. Considering the lens system of microscope, the minimum resolution is around 1 μm × 1 μm. Therefore, this plasmonic sensing system can be a quite powerful tool for the high resolution and the real time bio-detection. After acquisition of the color information from the image, color components, L*, a*, and b*, are extracted to be utilized as sensing factors (Fig. 1b-c) and used as the elements of our mathematical calculation model for the prediction of the refractive indices and transparent materials (Fig. 1d-e).

3.2. Correlation between spacing conditions and color components

The spacing of the plasmonic sensors is one of the crucial factors to determine the resonant peak position of the extraordinary light transmission spectrum. Our previous study demonstrated the optimal geometric conditions of nanostructures for the visible light filtering effect and the basic concept of bio-detection (Kim et al., 2016). In general, an increase in the spacing between the holes causes a red-shift in the resonant peak, and a decrease in the spacing causes a blue-shift (Fig. 2d). Additionally, the spectrums of the plasmonic sensors were changed by the different surrounding material (20% NaCl solution) which was even transparent. Therefore, the analysis of the spectrum change can be a good sensing mechanism of different transparent materials in the visible region for various applications. Some results published so far dealt with how to maximize this spectrum change or to enhance the detection ability of the difference. However, this detection ability requires a spectrometer resulting in a complicated measurement system with high cost. Additionally, to get the stable and reliable visible spectrum, it induces a spatial limit because the minimum detecting area is around 100 μm × 100 μm even with a good microscope. Therefore, a new approach to detect the refractive index change without a spectrometer should essentially guarantee some important merits including easy-to-use and simple measurement with low spatial limit. From this perspective, color analysis based on CIELAB could be a good candidate.

To confirm whether there is a particular trend between the nanohole spacing and CIELAB, the color components were extracted from the optical transmission images of our plasmonic sensors with spacing conditions of 275, 300, 325, 350, 375, 400, 425, 450, and 475 nm. As a result, at the visible light region, spacing-CIELAB characteristic curves were plotted as a high-order function that included several inflection points dividing the increasing and decreasing intervals (Fig. 3a) while the spacing-resonant wavelength characteristic curves show a linear relationship.(Kim et al., 2016) The different trends are due to the difference in the fundamental principles that determine the CIELAB values and the spectral properties as the spacing changes. The resonant wavelength of the extraordinary transmission resulting from the coupling of the incident light and surface plasmons is described as below (Ghaemi et al., 1998):

$$\lambda = \frac{s}{\sqrt{\frac{4}{3}(i^2 + ij + j^2)}} \sqrt{\frac{\varepsilon_d \varepsilon_m}{\varepsilon_d + \varepsilon_m}}, \tag{7}$$

where s is the spacing, and (i, j) is the scattering order. ε_d and ε_m are dielectric constants of the dielectric and metal. Eq. (7) shows how the spacing and the resonant wavelength of the transmission spectra are linearly related. On the other hand, it is difficult to expect the same amount of variations in the color components according to the increase and decrease of the spacing. As shown in Eqs. (4)–(6), L*, a*, and b* are described by different combinations of X, Y, and Z values which cover color channels such as black to white, green to red, and blue to yellow, respectively. It means that they are sensitive to the change in their own color channel and insensitive to others. Due to this reason, different L*, a*, and b* values in a single plasmonic sensor and different amounts of variations according to the change in the spacing with the same increment are observed (Fig. 3a). However, the spacing-CIELAB characteristic curves can be meaningful in designing a plasmonic sensor when the color sensitivity to the spacing shows some correlation with

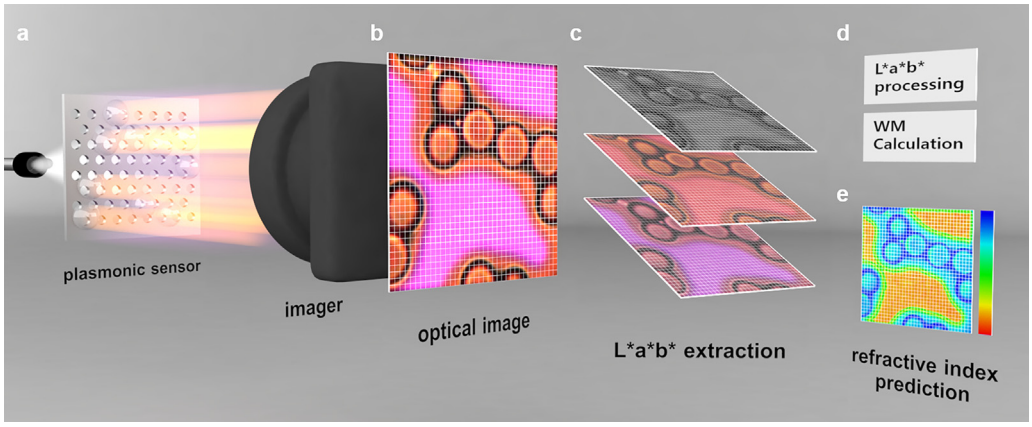

Fig. 1. Schematic of the color-sensitive and spectrometer-free sensing. (a–b) White light exposes to the plasmonic sensor with transparent materials. Characteristic colors resulting from the interaction of the sensor and its interface material are collected by an imager and recorded as an optical image. (c) Color components, L*, a*, and b*, of each pixel are extracted from the image. (d-e) The refractive indices are predicted through the CIELAB processing and the weighted mean calculation.

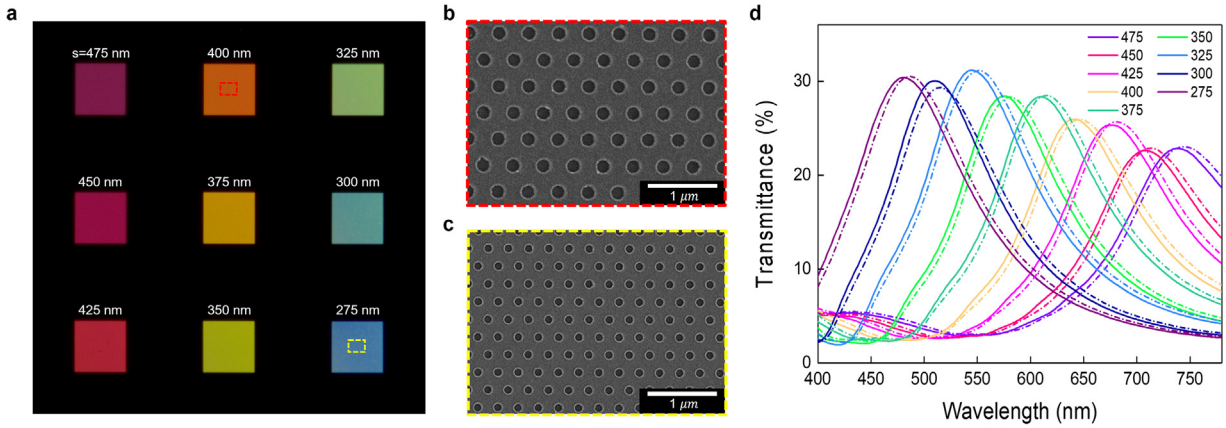

Fig. 2. (a) An optical microscope image of the plasmonic sensors with varying spacing conditions at 0% NaCl solution. (b–c) Scanning electron microscope images of the hexagonal nanohole arrays with 400 nm (b) and 275 nm (c) spacing conditions. (d) Transmission spectra of the plasmonic sensors at 0% (solid lines) and 20% (dash-dot lines) NaCl solution.

the color sensitivity to an optical parameter such as a refractive index. To confirm whether there is a certain correlation, the derivative (or instantaneous rate of change) of each color component for the nine spacing conditions and the change of each color component with respect to the increase of the refractive index for the nine plasmonic sensors are described together in Fig. 3b–d. Interestingly, the derivative and the change of the three color components for each spacing of the plasmonic sensors show a positive correlation. For example, both values of L* are positive at the 275, 300, and 325 nm spacing conditions and negative at the other spacing conditions. Moreover, the maximum and minimum values are commonly observed at the 275 and 400 nm spacing conditions. Such correlation between the derivative and the

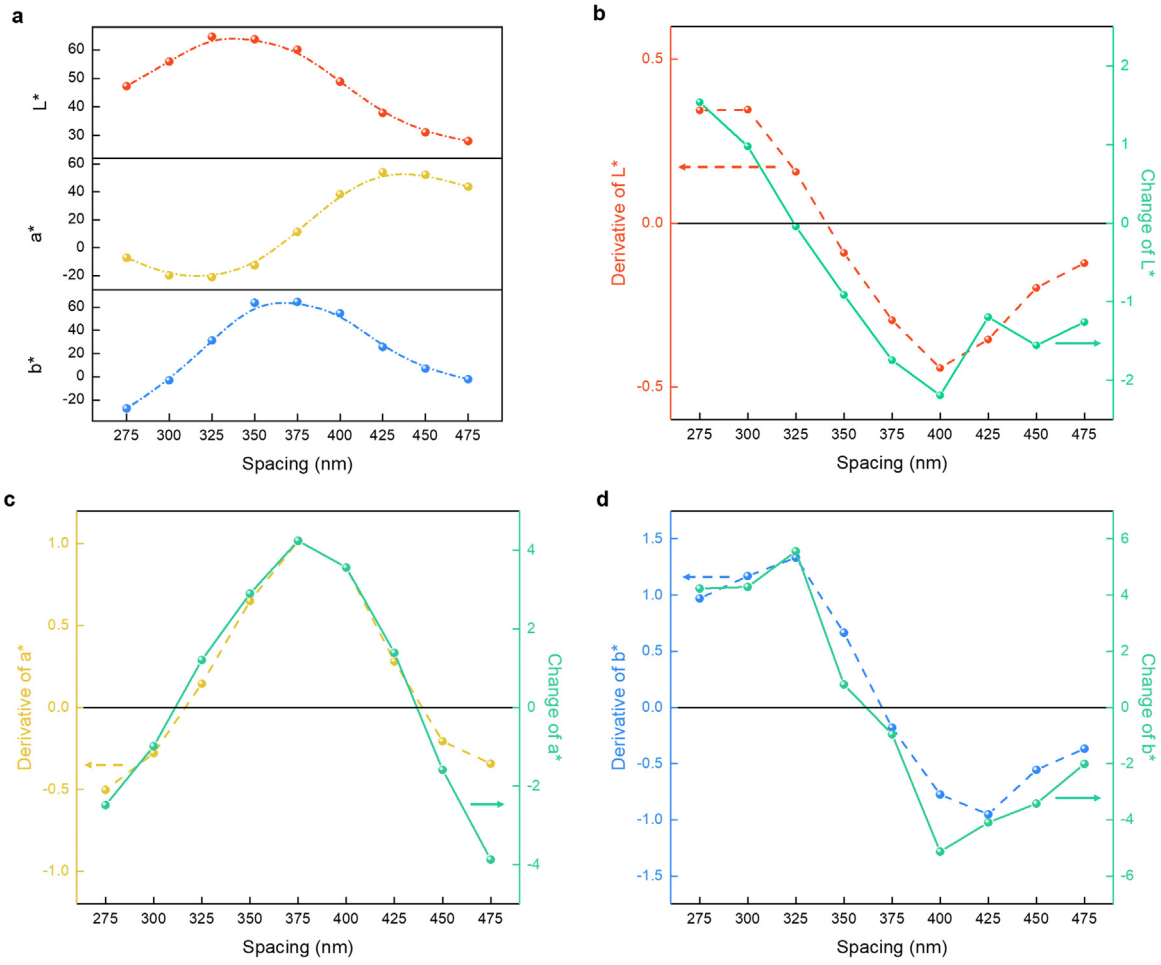

Fig. 3. The relationship between the spacing of the plasmonic sensors and the color components of CIELAB. (a) Measured (circles) and fitted (lines) L*(red), a*(yellow), and b*(blue) of the plasmonic sensors with 275, 300, 325, 350, 375, 400, 425, 450 and 475 nm spacing conditions at 0% NaCl solution. (b–d) Derivatives of L*(red), a*(yellow), and b*(blue) with respect to the spacing of the plasmonic sensors and the changes in the color components (solid green line) according to the change in the NaCl concentration from 0% to 20%.

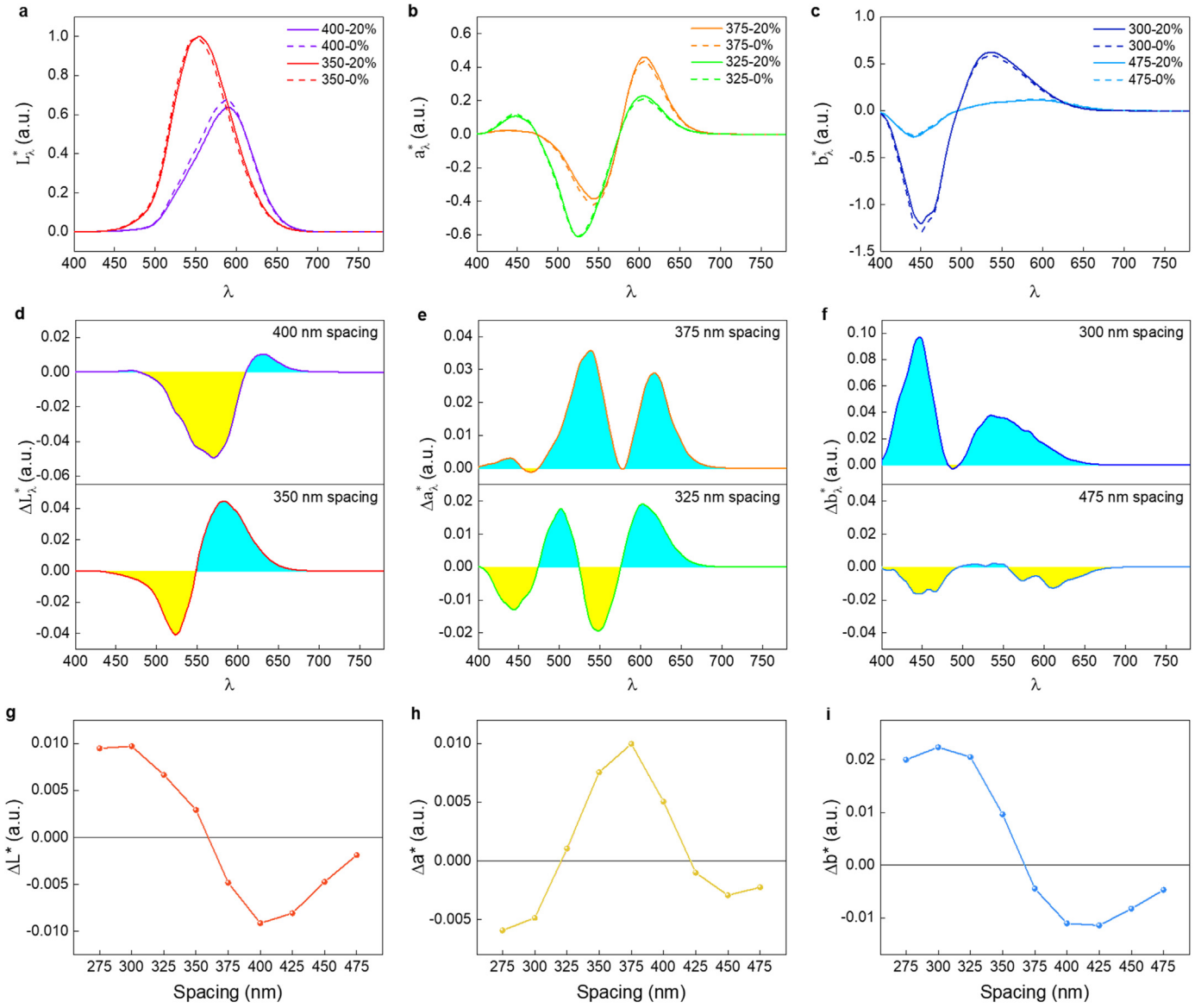

Fig. 4. (a–c) Normalized L_λ^* for the 400 and 350 nm spacing conditions (a), a_λ^* for the 375 and 325 nm spacing conditions (b), and b_λ^* for the 300 and 475 nm spacing conditions (c) before (dash line) and after (solid line) the increase in the concentration of NaCl solution from 0% to 20%. (d-f) Corresponding difference according to the increase in the concentrations. Positive and negative differences are filled with cyan and yellow colors, respectively. (g–i) Calculated and normalized changes in each color component, L*(g), a*(h), and b*(i) for the nine plasmonic sensors.

change is also valid for other color components shown in Fig. 3c–d. Thus, because the color sensitivity to the refractive index can be inferred from the color sensitivity to the spacing, a highly sensitive plasmonic sensor can be achieved by optimizing the geometric conditions of nanohole arrays and the analysis parameters.

To explain why the three color components of a single plasmonic sensor have different variations and why the same color component of each sensor show different sensitivities when a change in the refractive index occurs, we considered the mathematical models of XYZ (Eqs. 1–3) and CIELAB (Eqs. (4)–(6)). For this calculation, the transmission spectra of our nine plasmonic sensors in Fig. 2d were used. Additionally, to simply visualize the mathematical process, we graphed out $L_\lambda^* = Y_\lambda/Y_n$, $a_\lambda^* = X_\lambda/X_n - Y_\lambda/Y_n$, and $b_\lambda^* = Y_\lambda/Y_n - Z_\lambda/Z_n$. These simplified expressions are sufficient to reflect the variation aspects of each color component because of the fact that the L*, a*, and b* values are proportional to the increasing function $f(t)$, given as $\sqrt{t}$ ($t > 0.0089$) and $7.7870t + 0.1379$ ($t \leq 0.0089$), and its variables over all visible light range shown in Eqs. (4)–(6). Fig. 4a–c illustrates the normalized L_λ^*, a_λ^*, and b_λ^* values of several plasmonic sensors for deionized water based solutions with two different NaCl concentrations of 0% (dash line) and 20% (solid line). To understand what causes the different sensitivities of the color components, we selected the sensors which showed the maximum and minimum changes in Fig. 3b–d. For example, sensors with 375 and 325 nm spacing conditions were considered as the maximum and minimum changes for a_λ^*, respectively. The corresponding difference, ΔL_λ^*, Δa_λ^*, and Δb_λ^*, according to the increase in the refractive index as a function of λ are illustrated in Fig. 4d–f. Here, it can be noticed that the total integral value including the positive (cyan) and negative (yellow) areas means the total net change in the color component. The changes in the L*, a*, and b* values based on the mathematical models for the nine plasmonic sensors were obtained (Fig. 4g–i). Because it is expected that a large positive or negative integral results in high sensitivity, the plasmonic sensors with 400, 375, and 300 nm spacing conditions show large positive or negative changes in L*, a*, and b*, respectively. Therefore, from a theoretical point of view, the sensitivity is improved when the positive or negative area is large, and the offset of the positive and negative areas is minimized. The sensitivity from the calculation supports the experimental results in

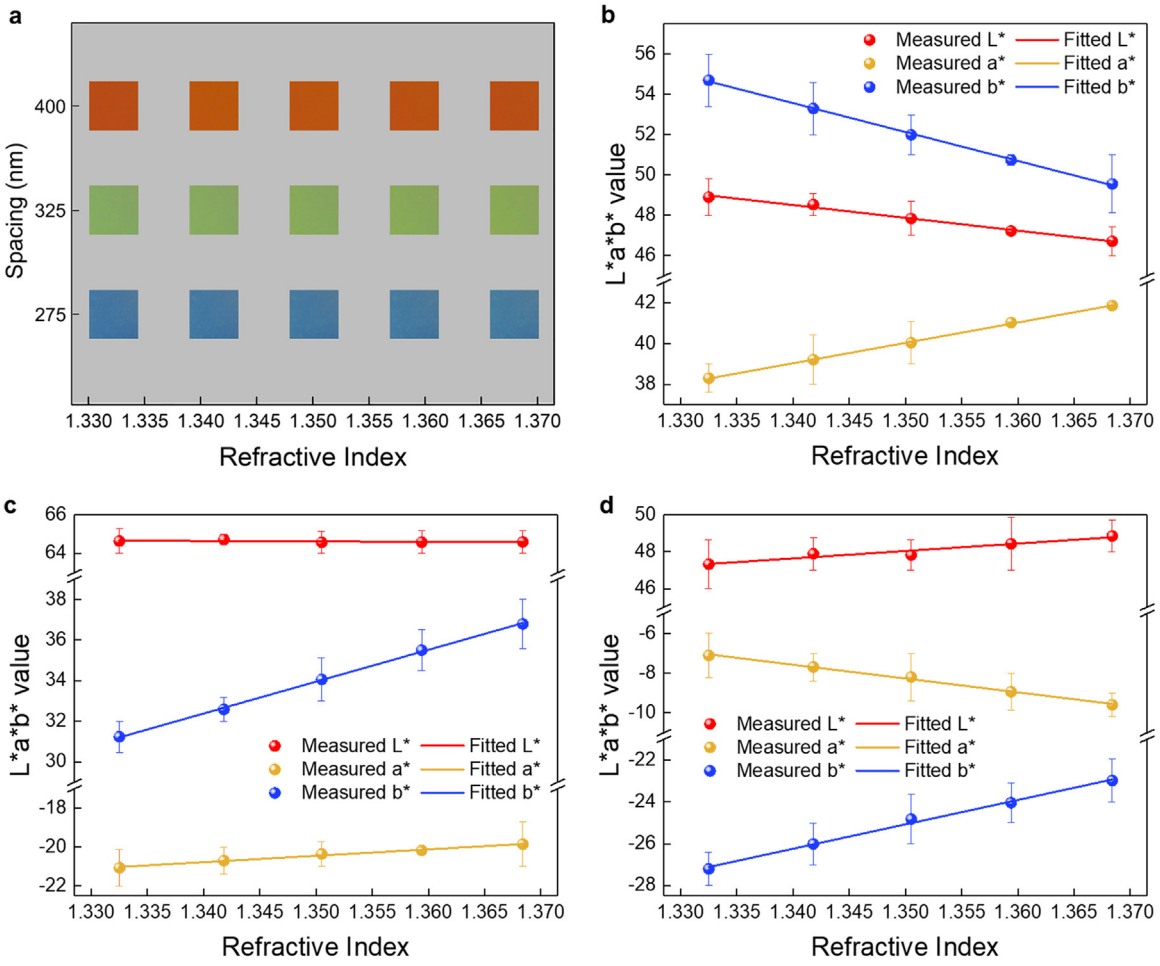

Fig. 5. (a) Optical microscope images with respect to the refractive index changes of the NaCl solutions for the plasmonic sensors with the spacing conditions of 400 nm, 325 nm, and 275 nm. (b–d) Corresponding color components for 400 nm (b), 325 nm (c), and 275 nm (d).

Fig. 3b–d for all the plasmonic sensors.

3.3. Prediction using color components and weighted mean calculation

As mentioned previously, if an optoelectronic property of optically transparent materials such as the refractive index is obtained by detecting the changes in the color components using plasmonic sensors, it could be advantageous for real-time and label-free bio-detection. To achieve our color-sensitive and spectrometer-free sensing platform, we tried to find the correlation between the refractive index and the individual sensing factor, L*, a*, and b*. As the first step, NaCl solutions with various concentrations (0%, 5%, 10%, 15%, and 20%) were prepared as various conditions of the refractive index (1.3325, 1.3418, 1.3505, 1.3594, and 1.3684). After obtaining optical images of the plasmonic sensors with the NaCl solutions using a CCD camera, the corresponding color responses were extracted from each (200 × 200 pixels) and statistically averaged. Fig. 5 describes the results of three plasmonic sensors with spacing conditions of 400, 325, and 275 nm. According to the experimentally measured and statistically calculated data, each sensor has different color sensitivities to the change in the refractive index. This is due to the different variation trends of the color components shown in Fig. 4. In addition, it can clearly be seen that there is a linear correlation between the sensing factor and the refractive index for all cases. Therefore, the sensitivity can be obtained from these relations. A plasmonic sensor with a spacing condition of 400 nm shows a color sensitivity of -63.58 RIU^{-1} for L*, 99.85 RIU^{-1} for a*, and -143.50 RIU^{-1} for b*(Fig. 5a). The other sensors with spacing conditions of 325 (Fig. 5b) and 275 nm (Fig. 5c) have sensitivities of -2.51 RIU^{-1} (L*), 32.84 RIU^{-1} (a*), 156.94 RIU^{-1} (b*), and 40.48 RIU^{-1} (L*), -69.52 RIU^{-1} (a*), 116.72 RIU^{-1} (b*), respectively. The sensitivity of the nine plasmonic sensors was also obtained from the measurement and calculation (Table S1). To evaluate the performance of our sensing method in terms of accuracy for all the plasmonic sensors, the mean absolute error (MAE) of the predicted refractive index using each color component, L*, a*, and b*, is calculated using the following equation:

$$\mathrm{MAE} = \frac{1}{mn}\sum_{k=1}^{m}\sum_{j=1}^{n}|p_{k,j} - r_k|, \tag{8}$$

where p and r indicate the refractive index predicted by each pixel and measured by a refractometer, respectively. The number of pixels and the refractive index conditions are denoted as $n = 40{,}000$ and $m = 5$ for this evaluation. The calculated MAE values for all L*, a*, and b* of the plasmonic sensors are listed in Table S1. As a result, the minimum MAE, 1.298×10^{-4} RIU, is achieved by the sensitivity of a* from the sensor with the 475 nm spacing. The MAE with respect to the sensitivity is described in Fig. 6a. There is a specific tendency that the MAE is gradually reduced when the sensitivity increases. This fact indicates that the prediction using our sensing platform is going to be more accurate as the sensitivity improves. In addition, the sensitivity of a* and b* is generally higher than that of L*. This trend agrees with the result that the derivatives of a* and b* are larger than that of L* shown in Fig. 3. As mentioned earlier, the plasmonic sensor structure makes the filtered color change depending on the surrounding environment, and therefore, one can infer that the a* and b* indices representing color are

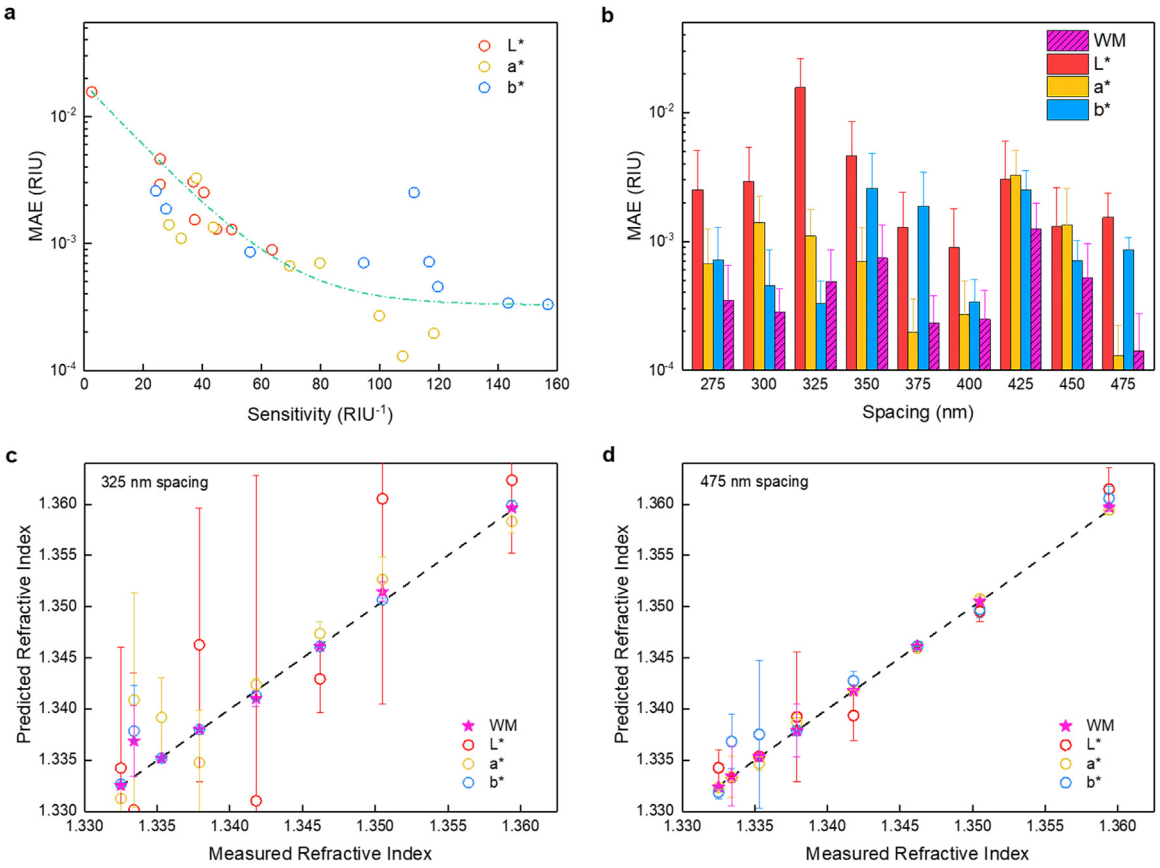

Fig. 6. (a) Mean absolute errors as a function of the color sensitivity. Sensitivities are obtained from the linear correlations of the individual color components for each plasmonic sensor and the refractive index. Mean absolute errors are calculated using the refractive indices given from the measured data and our plasmonic sensors for NaCl solutions with varying concentrations (0%, 5%, 10%, 15%, and 20%). Red, yellow, and blue circles represents the mean absolute errors of the prediction from the individual sensing index, L*, a*, and b*, respectively. (b) Comparison of the mean absolute errors based on the individual sensing factors (red, yellow, and blue bars) and the weighed mean calculations (striped magenta bar). (c–d) The refractive index prediction of unknown NaCl concentrations using the plasmonic sensors with the individual sensing factor and the weighted mean calculation. The refractive index of the NaCl solutions is given as 1.3325, 1.3334, 1.3353, 1.3379, 1.3418, 1.3462, 1.3505, and 1.3594. The results are for the plasmonic sensors with the spacing conditions of 325 nm (c) and 475 nm (d).

more sensitive than L* which generally corresponds to brightness. For this reason, it is effective to detect the refractive index using a* and b* when each color component is used as an individual sensing factor. However, obtaining multiple sensing factors from a single measurement of a single sensor and using them as variables for a function which induces a more stable sensing result are expected to show a more significant advantage in reducing prediction errors and enhancing accuracy. To derive a new prediction value from multiple factors, the weighted mean (WM) calculation is used as bellow:

$$\mathrm{WM} = \frac{\sum_{j=1}^{3} P_j e_j^{-1}}{\sum_{j=1}^{3} e_j^{-1}}, \tag{9}$$

where the indexed variable sequences, P_j and e_j, are the predicted refractive index and corresponding MAE for the individual sensing factors, L*, a*, and b*. The inverse of e is set as the weight so that, in the prediction, a sensing factor with a low error has a high contribution and a sensing factor with a high error has a low contribution. After the WM calculations, the prediction errors are obtained using Eq. (8). Fig. 6b shows the MAE values of the refractive indices predicted by the individual sensing factors (red, yellow, and blue bars) and the WM calculations (striped magenta bar). According to the results, in general, the prediction error of the WM calculations is lower than that of the individual sensing factors. In the prediction based on the WM calculation, the final result is mainly determined by sensing factors which have high weights. Therefore, it can be recognized that the prediction using the WM has generally reduced errors and an enhanced sensing performance. In addition, MAE values under 1×10^{-3} RIU are achieved for all the sensors.

Finally, to validate the sensing performance of our color-sensitive and spectrometer-free sensing platform based on plasmonic sensors and WM calculations, the unknown concentrations of NaCl solutions were predicted. For this experiment, the nine plasmonic sensors which had been used in the previous experiment, were surrounded by NaCl solutions at several concentrations, 0%, 0.5%, 1.5%, 3%, 5%, 7.5%, 10%, and 15%. The corresponding refractive indices of the NaCl solutions are 1.3325, 1.3334, 1.3353, 1.3379, 1.3418, 1.3462, 1.3505, and 1.3594, respectively. The individual sensing factors, L*, a*, and b*, were statistically extracted and converted into refractive indices using our linear correlation models. Then, they were used as variables in the WM calculation. Fig. 6c–d shows the predicted refractive index using the individual sensing factors and WM calculations. Among the individual sensing factors, L* of a sensor with 325 nm spacing shows the poorest results, whereas a* of a sensor with 475 nm spacing has the most accurate prediction results. As expected, predictions using a sensing factor that has the highest MAE above 1×10^{-2} RIU are relatively inaccurate while a factor that has the lowest MAE shows a result which is almost consistent with the measured refractive indices. When the WM calculation is used as a prediction tool, the prediction accuracy is more enhanced, and the MAE is reduced for all the sensors. For example, when using the WM calculation, a plasmonic sensor with a 475 nm spacing condition can detect the difference in the refractive index of up to 0.0009. Therefore, a good performance can be expected if an individual sensing factor with a low MAE is used, and it can be seen that it is more

advantageous to predict the refractive index with the WM calculation. The predicted refractive indices of the nine plasmonic sensors based on the WM calculation are described in Fig. S2.

To establish the color-sensitive and spectrometer-free sensing platform, the color sensitivity of plasmonic sensors is most important because the change in the refractive index causes different changes in the color components. Therefore, selecting the proper material and geometric conditions of plasmonic sensors, which show large changes in L*, a*, and b*, is necessary to obtain a high sensitivity and low prediction error. Our study found and optimized the sensing conditions with experimental and mathematical analysis.

4. Conclusion

In summary, we have demonstrated the color-sensitive analysis method for enhanced bio-detecting performance including the sensitivity and the accuracy. Detailed study on a trend of each color component according to the spacing of plasmonic sensors shows a high correlation between the derivative of the color component for the spacing of plasmonic sensors and the color sensitivity to the refractive index. This correlation enables to design and fabricate highly sensitive plasmonic sensors consisted of nanohole array structures. In addition, by utilizing all color components of CIELAB as an individual sensing factor, the color sensitivity up to 156.94 RIU^{-1} and the minimum MAE up to 1.298×10^{-4} RIU are achieved. The WM calculation further improves the sensing performance as using L*, a*, and b* sensing factors simultaneously for the prediction of the refractive index. As a result, the difference in the refractive index of only 0.0009 is detected and the prediction error is reduced below 1×10^{-3} RIU. The suggested color-sensitive and spectrometer-free sensing platform only needs a low magnification lens and a CCD camera making the measurement system simple and cost-effective. In this sense, a color-sensitive and spectrometer-free sensing presented in this study could help to detect not only the refractive index of liquid solutions but also biomaterials without complex systemic and time-consuming preparation. Our work opens great potential of color-sensitive analysis going to the significantly high sensitivity and high resolution. Therefore, we expect that more sensitive plasmonic structures and more effective mathematical processes will increase the practical availability in medical and biological fields.

Acknowledgements

This study was supported by the Basic Science Research Program through National Research Foundation of Korea (NRF) funded by the MSIT (2014M3A9D7070668, 2015R1A2A2A01005054, and 2017M3A9G8084463) and DGIST R&D Program of MSIT (18-BD-0404).

Appendix A. Supplementary material

Supplementary data associated with this article can be found in the online version at https://doi.org/10.1016/j.bios.2018.11.048.

Appendix B. Supplementary material

Supplementary data associated with this article can be found in the online version at https://doi.org/10.1016/j.bios.2018.11.048.

References

Bae, K., Lee, J., Kang, G., Yoo, D.-S., Lee, C.-W., Kim, K., 2015. Refractometric and colorimetric index sensing by a plasmon-coupled hybrid AAO nanotemplate. RSC Adv. 5 (125), 103052–103059.

Ballard, Z.S., Shir, D., Bhardwaj, A., Bazargan, S., Sathianathan, S., Ozcan, A., 2017. Computational sensing using low-cost and mobile plasmonic readers designed by machine learning. ACS Nano 11 (2), 2266–2274.

Baquedano, E., Gonzalez, M.U., Paniagua-Dominguez, R., Sanchez-Gil, J.A., Postigo, P.A., 2017. Low-cost and large-size nanoplasmonic sensor based on Fano resonances with fast response and high sensitivity. Opt. Express 25 (14), 15967–15976.

Beck, F.J., Polman, A., Catchpole, K.R., 2009. Tunable light trapping for solar cells using localized surface plasmons. J. Appl. Phys. 105 (11), 114310.

Burgos, S.P., Yokogawa, S., Atwater, H.A., 2013. Color imaging via nearest neighbor hole coupling in plasmonic color filters integrated onto a complementary metal-oxide semiconductor image sensor. ACS Nano 7 (11), 10038–10047.

Cetin, A.E., Coskun, A.F., Galarreta, B.C., Huang, M., Herman, D., Ozcan, A., Altug, H., 2014. Handheld high-throughput plasmonic biosensor using computational on-chip imaging. Light Sci. Appl. 3, e122.

Chang, T.Y., Huang, M., Yanik, A.A., Tsai, H.Y., Shi, P., Aksu, S., Yanik, M.F., Altug, H., 2011. Large-scale plasmonic microarrays for label-free high-throughput screening. Lab Chip 11 (21), 3596–3602.

Chen, P., Chung, M.T., McHugh, W., Nidetz, R., Li, Y., Fu, J., Cornell, T.T., Shanley, T.P., Kurabayashi, K., 2015. Multiplex serum cytokine immunoassay using nanoplasmonic biosensor microarrays. ACS Nano 9 (4), 4173–4181.

Coskun, A.F., Cetin, A.E., Galarreta, B.C., Alvarez, D.A., Altug, H., Ozcan, A., 2014. Lensfree optofluidic plasmonic sensor for real-time and label-free monitoring of molecular binding events over a wide field-of-view. Sci. Rep. -UK 4, 6789.

Ghaemi, H., Thio, T., Grupp, D., Ebbesen, T.W., Lezec, H., 1998. Surface plasmons enhance optical transmission through subwavelength holes. Phys. Rev. B 58 (11), 6779.

Homola, J., Dostálek, J., Chen, S., Rasooly, A., Jiang, S., Yee, S.S., 2002. Spectral surface plasmon resonance biosensor for detection of staphylococcal enterotoxin B in milk. Int. J. Food Microbiol. 75 (1), 61–69.

Im, H., Shao, H., Park, Y.I., Peterson, V.M., Castro, C.M., Weissleder, R., Lee, H., 2014. Label-free detection and molecular profiling of exosomes with a nano-plasmonic sensor. Nat. Biotechnol. 32 (5), 490.

Jackman, J.A., Linardy, E., Yoo, D., Seo, J., Ng, W.B., Klemme, D.J., Wittenberg, N.J., Oh, S.H., Cho, N.J., 2016. Plasmonic nanohole sensor for capturing single virus-like particles toward virucidal drug evaluation. Small 12 (9), 1159–1166.

Kabashin, A.V., Evans, P., Pastkovsky, S., Hendren, W., Wurtz, G.A., Atkinson, R., Pollard, R., Podolskiy, V.A., Zayats, A.V., 2009. Plasmonic nanorod metamaterials for biosensing. Nat. Mater. 8, 867.

Kim, S., Shin, J.H., Kim, S., Yoo, S.-J., Jun, B.O., Moon, C., Jang, J.E., 2016. Geometric effects of nano-hole arrays for label free bio-detection. RSC Adv. 6 (11), 8935–8940.

Lee, Y., Park, M.K., Kim, S., Shin, J.H., Moon, C., Hwang, J.Y., Choi, J.C., Park, H., Kim, H.R., Jang, J.E., 2017. Electrical broad tuning of plasmonic color filter employing an asymmetric-lattice nanohole array of Metasurface controlled by polarization rotator. ACS Photonics 4 (8), 1954–1966.

Li, J., Ye, J., Chen, C., Hermans, L., Verellen, N., Ryken, J., Jans, H., Van Roy, W., Moshchalkov, V.V., Lagae, L., 2015. Biosensing using diffractively coupled plasmonic crystals: the figure of merit revisited. Adv. Opt. Mater. 3 (2), 176–181.

Lin, E.-H., Tsai, W.-S., Lee, K.-L., Lee, M.-C.M., Wei, P.-K., 2017. Enhancing angular sensitivity of plasmonic nanostructures using mode transition in hexagonal gold nanohole arrays. Sens. Actuat. B-Chem. 241, 800–805.

LingáZheng, L., FeiáGao, P., ZhiáHuang, C., 2016. HSI colour-coded analysis of scattered light of single plasmonic nanoparticles. Nanoscale 8 (22), 11467–11471.

Liu, B., Chen, S., Zhang, J., Yao, X., Zhong, J., Lin, H., Huang, T., Yang, Z., Zhu, J., Liu, S., 2018. A Plasmonic sensor array with ultrahigh figures of merit and resonance Linewidths down to 3 nm. Adv. Mater. 30 (12), 1706031.

Na, H.-K., Wi, J.-S., Son, H.Y., Ok, J.G., Huh, Y.-M., Lee, T.G., 2018. Discrimination of single nucleotide mismatches using a scalable, flexible, and transparent three-dimensional nanostructure-based plasmonic miRNA sensor with high sensitivity. Biosens. Bioelectron. 113, 39–45.

Park, B., Yun, S.H., Cho, C.Y., Kim, Y.C., Shin, J.C., Jeon, H.G., Huh, Y.H., Hwang, I., Baik, K.Y., Lee, Y.I., Uhm, H.S., Cho, G.S., Choi, E.H., 2014. Surface plasmon excitation in semitransparent inverted polymer photovoltaic devices and their applications as label-free optical sensors. Light Sci. Appl. 3, e222.

Sriram, M., Markhali, B.P., Nicovich, P.R., Bennett, D.T., Reece, P.J., Hibbert, D.B., Tilley, R.D., Gaus, K., Vivekchand, S., Gooding, J.J., 2018. A rapid readout for many single plasmonic nanoparticles using dark-field microscopy and digital color analysis. Biosens. Bioelectron. 117, 530–536.

Tseng, M.L., Yang, J., Semmlinger, M., Zhang, C., Nordlander, P., Halas, N.J., 2017. Two-dimensional active tuning of an aluminum plasmonic array for full-spectrum response. Nano Lett. 17 (10), 6034–6039.

Yanik, A.A., Huang, M., Kamohara, O., Artar, A., Geisbert, T.W., Connor, J.H., Altug, H., 2010. An optofluidic nanoplasmonic biosensor for direct detection of live viruses from biological media. Nano Lett. 10 (12), 4962–4969.

Zafar, R., Salim, M., 2015. Enhanced figure of merit in Fano resonance-based plasmonic refractive index sensor. IEEE Sens. J. 15 (11), 6313–6317.

Zhang, D., Lu, Y., Jiang, J., Zhang, Q., Yao, Y., Wang, P., Chen, B., Cheng, Q., Liu, G.L., Liu, Q., 2015. Nanoplasmonic biosensor: Coupling electrochemistry to localized surface plasmon resonance spectroscopy on nanocup arrays. Biosens. Bioelectron. 67, 237–242.

Zhou, B., Xiao, X., Liu, T., Gao, Y., Huang, Y., Wen, W., 2016. Real-time concentration monitoring in microfluidic system via plasmonic nanocrescent arrays. Biosens. Bioelectron. 77, 385–392.